Research Article | Vol. 8, No. 2 | 1 Feb 2017 | BIOMEDICAL OPTICS EXPRESS 873

Biomedical Optics EXPRESS

Continuous multi-modality brain imaging reveals modified neurovascular seizure response after intervention

Dene Ringuette,[1] Melanie A. Jeffrey,[2] Suzie Dufour,[1,2] Peter L. Carlen,[1,2] and Ofer Levi[1,3,*]

[1]*The Institute of Biomaterials and Biomedical Engineering, University of Toronto, 164 College Street, Toronto, Ontario, M5S 3G9, Canada*
[2]*Division of Fundamental Neurobiology, Toronto Western Research Institute, 60 Leonard Ave, Toronto, Ontario M5T 2R1, Canada*
[3]*The Edward S. Rogers Sr. Department of Electrical and Computer Engineering, University of Toronto, 10 King's College Road, Toronto, Ontario, M5S 3G4, Canada*
[*]*ofer.levi@utoronto.ca*

Abstract: We developed a multi-modal brain imaging system to investigate the relationship between blood flow, blood oxygenation/volume, intracellular calcium and electrographic activity during acute seizure-like events (SLEs), both before and after pharmacological intervention. Rising blood volume was highly specific to SLE-onset whereas blood flow was more correlated with all eletrographic activity. Intracellular calcium spiked between SLEs and at SLE-onset with oscillation during SLEs. Modified neurovascular and ionic SLE responses were observed after intervention and the interval between SLEs became shorter and more inconsistent. Comparison of artery and vein pulsatile flow suggest proximal interference and greater vascular leakage prior to intervention.

OCIS codes: (110.4234) Multispectral and hyperspectral imaging; (110.6150) Speckle imaging; (170.2520) Fluorescence microscopy.

References and links

1. B. Hermann and M. Seidenberg, "Epilepsy and cognition," Epilepsy Currents **7**, 1–6 (2007).
2. A. Bonora, F. Benuzzi, G. Monti, L. Mirandola, M. Pugnaghi, P. Nichelli, and S. Meletti, "Recognition of emotions from faces and voices in medial temporal lobe epilepsy," Epilepsy Behav. **20**, 648–654 (2011).
3. N. Adachi, T. Hara, Y. Oana, M. Matsuura, Y. Okubo, N. Akanuma, M. Ito, M. Kato, and T. Onuma, "Difference in age of onset of psychosis between epilepsy and schizophrenia," Epilepsy Res. **78**, 201–206 (2008).
4. P. Tian, I. C. Teng, L. D. May, R. Kurz, K. Lu, M. Scadeng, E. M. Hillman, A. J. De Crespigny, H. E. D'Arceuil, J. B. Mandeville *et al.*, "Cortical depth-specific microvascular dilation underlies laminar differences in blood oxygenation level-dependent functional MRI signal," Proc. Natl. Acad. Sci **107**, 15246–15251 (2010).
5. D. J. Rossi, "Another bold role for astrocytes: coupling blood flow to neural activity," Nat. Neurosci **9**, 159–161 (2006).
6. P. Bazzigaluppi, S. Dufour, and P. L. Carlen, "Wide field fluorescent imaging of extracellular spatiotemporal potassium dynamics in vivo," NeuroImage **104**, 110–116 (2015).
7. P. L. Carlen, N. Gurevich, and P. Polc, "Low-dose benzodiazepine neuronal inhibition: enhanced ca 2+-mediated k+-conductance," Brain research **271**, 358–364 (1983).
8. S. Bahar, M. Suh, M. Zhao, and T. H. Schwartz, "Intrinsic optical signal imaging of neocortical seizures: the 'epileptic dip'," Neuroreport **17**, 499–503 (2006).
9. M. Zhao, M. Suh, H. Ma, C. Perry, A. Geneslaw, and T. H. Schwartz, "Focal increases in perfusion and decreases in hemoglobin oxygenation precede seizure onset in spontaneous human epilepsy," Epilepsia **48**, 2059–2067 (2007).
10. M. Zhao, J. Nguyen, H. Ma, N. Nishimura, C. B. Schaffer, and T. H. Schwartz, "Preictal and ictal neurovascular and metabolic coupling surrounding a seizure focus," J. Neurosci **31**, 13292–13300 (2011).
11. M. Zhao, H. Ma, M. Suh, and T. H. Schwartz, "Spatiotemporal dynamics of perfusion and oximetry during ictal discharges in the rat neocortex," J. Neurosci **29**, 2814–2823 (2009).
12. M. B. Bouchard, B. R. Chen, S. A. Burgess, and E. M. C. Hillman, "Ultra-fast multispectral optical imaging of cortical oxygenation, blood flow, and intracellular calcium dynamics," Opt. Express **17(18)**, 15670–8 (2009).
13. H. Ma, M. Zhao, and T. H. Schwartz, "Dynamic neurovascular coupling and uncoupling during ictal onset, propagation, and termination revealed by simultaneous in vivo optical imaging of neural activity and local blood volume," Cerebral Cortex **23(4)**, 885–899 (2013).

#278125 http://dx.doi.org/10.1364/BOE.8.000873
Journal © 2017 Received 4 Oct 2016; revised 5 Dec 2016; accepted 19 Dec 2016; published 17 Jan 2017

Biomedical Optics EXPRESS

14. H. Ma, S. Harris, R. Rahmani, C. O. Lacefield, M. Zhao, A. G. Daniel, Z. Zhou, R. M. Bruno, J. Berwick, and T. H. Schwartz, "Wide-field in vivo neocortical calcium dye imaging using a convection-enhanced loading technique combined with simultaneous multiwavelength imaging of voltage-sensitive dyes and hemodynamic signals," Neurophotonics **1**, 015003 (2014).
15. S. Mennerick, M. Chisari, H.-J. Shu, A. Taylor, M. Vasek, L. N. Eisenman, and C. F. Zorumski, "Diverse voltage-sensitive dyes modulate $GABA_A$ receptor function," J. Neurosci **30**, 2871–2879 (2010).
16. H. Levy, D. Ringuette, and O. Levi, "Rapid monitoring of cerebral ischemia dynamics using laser-based optical imaging of blood oxygenation and flow," Biomed. Opt. Express **3**, 777–791 (2012).
17. L. M. Richards, E. L. Towle, D. J. Fox, and A. K. Dunn, "Intraoperative laser speckle contrast imaging with retrospective motion correction for quantitative assessment of cerebral blood flow," Neurophotonics **1**, 015006 (2014).
18. E. A. Munro, H. Levy, D. Ringuette, T. D. O'Sullivan, and O. Levi, "Multi-modality optical neural imaging using coherence control of VCSELs," Opt. Express **19**, 10747–10761 (2011).
19. C. Kamath, "A new approach to detect epileptic seizures in electroencephalograms using teager energy," ISRN Biomedical Engineering **2013** (2013).
20. R. Yadav, R. Agarwal, and M. Swamy, "Detection of epileptic seizures in stereo-EEG using frequency-weighted energy," in *50th Midwest Symposium on Circuits and Systems,* (IEEE, 2007), pp. 77–80.
21. D. Ringuette, M. A. Jeffrey, P. L. Carlen, and O. Levi, "Multi-modal in vivo imaging of brain blood oxygenation, blood flow and neural calcium dynamics during acute seizures," Proc. SPIE **9690**, 969011 (2016).
22. D. Ringuette, P. Carlen, and O. Levi, "Multi-modality optical imaging of temporal and spatial dynamics during in vivo seizure-like activity," in *Biomedical Optics 2016*, OSA Technical Digest (online), (Optical Society of America, 2016), paper BM4D–3.
23. S. Dufour, Y. Atchia, R. Gad, D. Ringuette, I. Sigal, and O. Levi, "Evaluation of laser speckle contrast imaging as an intrinsic method to monitor blood brain barrier integrity," Biomed. Opt. Express **4**, 1856–1875 (2013).

1. Introduction

Epilepsy is a condition in which an individual suffers from recurrent seizures that can lead to cognitive deficits [1], deficits in emotional recognition [2] and, in some cases, to psychosis [3]. A seizure is a state of hyper-synchronous neural activity in which a large population of neurons are recurrently activated. This leads to increased energy consumption and greater demand for oxygen and glucose. Through an adaptive response, neurovascular coupling (NVC)-induced vasodilation increases the local blood flow to meet this demand. In response to sensory-induced neural activity, NVC has been shown to produce changes in arteriole diameter of 5–25% [4]. Astrocytes are believed to be mediators of NVC and conduct this signal from the synapse to the vascular endothelial cells via a wave of increased intracellular calcium concentration ($[Ca^{2+}]_i$) [5]. Much remains unknown about NVC and how it might be modified by disease. Acute models of seizure in rodents have proven to be highly useful tools for investigating epilepsy. One common model is direct tissue application of the K^+ channel blocker 4-aminopyridine (4-AP) [6]. This promotes neural hyperactivity leading to seizure-like events (SLEs) and to intermittent electrical spikes between SLEs referred to as interictal epileptiform discharges (IEDs). Conversely, members of the benzodiazepine drug family, such as lorazepam (LZP) or midazolam, inhibit neural activity by increasing Cl^- conductance associated with γ-aminobutyric acid (GABA) binding and augmenting Ca^{2+}-mediated K^+ conduction [7].

Optical imaging has been a useful tool for investigating NVC. Experimental and clinical works, using intrinsic optical signal imaging (IOSI), indicate that changes in blood volume precede changes in the electrical component of seizure [8, 9]. Such blood volume changes require vasodilation events which were confirmed with two-photon laser-scanning microscopy (TPLSM) imaging of the focal 4-AP model [10] in which changes in vessel inner diameter of ~80% were observed within the seizure onset zone. Difficulty in obtaining simultaneous IOSI with laser Doppler measurements of blood flow have limited the capacity for comparison of the relationship between blood flow and oxygenation/volume [11]. Multi-modal imaging provides the opportunity to define the dynamical relations between physiological parameters. Recently, simultaneous calcium-sensitive fluorescent dye imaging (CSFDI) and single-wavelength IOSI have been used for *in vivo* mapping of the ionic and vascular changes associated with electrical hindpaw stimulation [12]. In this study, the system used alternating cyan- and green-light-

Biomedical Optics EXPRESS

emitting diode (LED) illumination sources with spectral narrowing optical filters for time-shared CSFDI and IOSI, respectively. The IOSI wavelength was chosen such that reflectance changes corresponded to changes in blood volume (*i.e.,* total hemoglobin (HbT)) and not blood oxygen saturation. This design was emulated by subsequent researchers applying multi-modal imaging to the study of SLEs. Initially, simultaneous voltage-sensitive dye (VSD) imaging and single-wavelength IOSI were used to investigate SLEs induced with focal 4-AP injection [13]. The VSD imaging was done in 20–40 second bursts to maximize temporal resolution and limit photo-bleaching. This work revealed that the majority of SLEs begin with an initial voltage spike event [13]. In a subsequent work [14], time-shared CSFDI and dual-wavelength IOSI were used to measure changes in oxyhemoglobin (HbO_2) and deoxyhemoglobin (HbR) during SLEs. In their direct comparison, CSFDI provided more distinct information than VSD imaging, with the latter more closely mimicking the local field potential (LFP). This redundancy, combined with the fact that the most common VSDs have been shown to modulate $GABA_A$ receptor functionality [15], suggests that CSFDI is better suited for investigating pharmacological intervention from SLEs with drugs such as benzodiazepines. These pioneering studies have opened an approach to investigating SLE dynamics, which is currently under-investigated with respect to both system flexibility and the investigation of drug interaction.

In this work, we investigate the relationship between blood flow, blood oxygenation and $[Ca^{2+}]_i$ dynamics during 4-AP induced SLEs. In addition, we investigate the change in this relationship during pharmacological intervention using LZP. We sought to improve upon previous multi-modal systems by integrating high-temporal resolution full-field blood flow imaging provided by laser speckle contrast imaging (LSCI). We used coherence modulation of near-infrared (NIR) vertical-cavity surface-emitting lasers (VCSELs) to achieve simultaneous three-wavelength IOSI and LSCI, similar to our previous work [16]. The NIR imaging system was adapted to a conventional Epifluorescent microscope for simultaneous CSFDI on a separate camera (to avoid time-sharing, enabling higher temporal resolution and to permit independent channel optimization). Our chosen integration approach enabled the use of high numerical aperture (NA) water immersion objective lens in addition to a wide field-of-view (FOV) imaging approach typically used for SLE imaging. These three imaging modalities have not previously been implemented simultaneously *in vivo*. Furthermore, none of these optical imaging modalities have been applied to *in vivo* imaging of SLEs during pharmacological intervention. We used an LFP-derived measure of SLE-activity, which we found empirically to be highly correlated with our optically based measures of SLEs, to infer the rate of optical signal response to SLEs and determine the consistency between SLE-onset and -termination. We exploited continuous fast blood flow imaging with electrocardiography (ECG) synchronization to produce high temporal resolution pulsation flow profiles. The temporal resolution of our flow profiles enabled greater pulsation correction for LSCI than previously reported [17] and allowed us to investigate changes in arterial and venous interaction dynamics in response to pharmacological intervention.

2. Methods

In this section we describe our multi-modal imaging system (see Fig. 1), surgical protocol, imaging procedure and analysis approach. Optical imaging modalities were integrated with electrographic recording of the LFP: LSCI measured changes in blood flow, IOSI measured concentration changes in oxy-, deoxy-, and total-hemoglobin, and CSFDI measured $[Ca^{2+}]_i$.

2.1. Imaging system

We adapted an Olympus BX61WI microscope for simultaneous back reflectance NIR-imaging (both LSCI and IOSI) and wide-field CSFDI (see Fig. 1(a)). We utilized a 40× immersion objective lens (Olympus LUMPlanFl/IR, NA = 0.8) designed for NIR and visible wavelength imaging and a 20× immersion objective lens (Olympus UMPlanFL N, NA = 0.5) in a subset of

Biomedical Optics EXPRESS

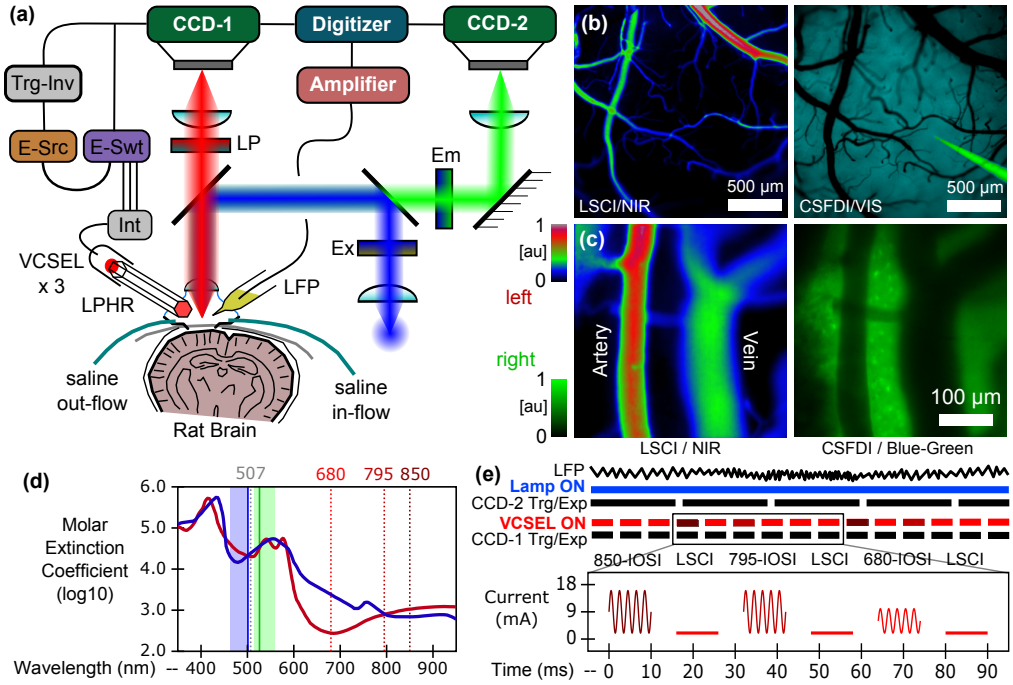

Fig. 1. Multi-modality rodent optical imaging system. **(a)** System diagram showing separate light paths and synchronization with LFP recording. *Legend:* CCD-1&2: cameras for NIR imaging and CSFDI, respectively, Trg-Inv: trigger inverter, E-Src & E-Swt: current source and switch, respectively, Ex/Em: CSFDI band-pass filters, LP: long-pass filter and dichroic mirror, Int: pin adapter interface, and VCSEL and LPHR comprise the NIR illumination module. **(b)** Large FOV images from LSCI (left) and CSFDI (right) just prior to dye injection (4× mag.) **(c)** Small FOV images from LSCI (left) and CSFDI (right) after dye injection (20× mag). **(d)** Relative spectrum of CSFDI and multi-modal NIR imaging. Fluorescent cube ex/em band-pass indicated by blue/green regions, respectively. The darker blue/green vertical lines correspond to the dye ex/em maximum. The dotted red lines show the VCSEL wavelengths. **(e)** Modality synchronization and current switching sequence for VCSELs.

experiments. A 4× air-immersion objective lens (XLFluor4x/340, NA=0.28) was used for region-of-interest (ROI) selection and probe alignments (see Fig. 1(b), note: minimal auto-fluorescent background). A 20× magnification image of blood flow and fluorescence labeled cells is shown in Fig. 1(c). The left panel shows a map of blood flow from LSCI. The relative blood flow differences between arteries and veins become more discernible due to reduced depth of field (DOF). The right panel shows the fluorescently labeled cells in the cortex from CSFDI.

Oblique NIR illumination was provided using a multi-wavelength VCSEL package (Vixar, Inc. – 680 nm, 795 nm, and 850 nm). The spectral correspondence to HbO_2 and HbR adsorption is shown in Fig. 1(d). To minimize the effect of fluid surface movement, the VCSELs were coupled to a light pipe homogenizing rod (LPHR) (Edmond optic, #48-582) such that the free end of the LPHR could be immersed alongside the objective lens. The NIR and visible light paths were separated with a 660 nm long-pass dichroic mirror and filter for simultaneous acquisition. A fluorescein isothiocyanate (FITC) optimized filter cube with a Mercury arc lamp in an Epifluorescence configuration were used for CSFDI (see Fig. 1(a,d)). The NIR images were recorded at 62.5 Hz (10 ms exposure, 2×2 pixel binning) using a QImaging Rolera EMC^2 CCD camera. The CSFDI images were recorded at 20 Hz (50 ms exposure, 4×4 pixel binning) using a

Biomedical Optics EXPRESS

QImaging Retiga 4000R CCD Camera. We used a ~100% duty cycle to avoid shuttering while limiting photo-bleaching in the CSFDI channel. The camera exposure acquisition triggers were used to synchronize the different VCSEL illumination modes, as previously described in [16]. The VCSEL sources were electrically driven using a Keithley 6221 current source. The individual VCSELs were toggled using a Keithley 7001 electrical current switch system. A driving current profile and source correspondence was repeated every six frames (see Fig. 1(e)). In every second frame a 680 nm VCSEL was driven near threshold producing a single-mode of coherent illumination suitable for LSCI. In the alternate set of frames, the driving current to the active VCSEL was rapidly modulated producing a sequence of higher-order (lower coherence) modes which result in more uniform illumination better suited for IOSI [18]. The central illumination wavelengths of IOSI frames were toggled between 850 nm, 795 nm and 680 nm.

Thermally-pulled glass electrodes with a chloride-coated silver core were used for LFP recording. The LFP electrodes were filled with Oregon Green® 488 BAPTA-1, AM, cell permeant, fluorescent dye-based labeled calcium indicator (50 μg in 20 μL of Pluronic F-127 in dimethyl sulfoxide (DMSO) subsequently dissolved in 200 μL of saline 0.9% NaCl). The LFP electrodes were then connected to a headstage pre-amplifier (Axon Instruments (AI), CV 203BU) mounted on a micromanipulator (Burleigh, PCS-5000 series). Subsequent analog amplification was performed using an Integrated patch clamp (AI, AxoPatch 200B). In some experiments, a duplicate second LFP recording channel was used with the electrode alignment roughly perpendicular to the first channel. The LPHR was oriented roughly perpendicular to one electrode and antiparallel to the other, to minimize reflection and lensing of the incident NIR light. The electrodes for ECG recording were connected to an analog pre-amplifier (AI, HS-2A) and amplifier (AI, AxoClamp-2B). The output of each electrical amplifier was recorded using a multi-channel digitizer (AI, DigiData 1322A). The acquisition triggers of both cameras were each recorded using the same digitizer to synchronize the imaging modalities with each other and the LFP (see Fig. 1(e)). In post-processing each frame was time stamped using its acquistion trigger midpoint. The sampling rate of all channels was 16.7 kHz (10^6/min), enabling 60 μs timing precision in modality correlation. In some experiments, an active high-pass filter with cut-off frequency 0.1 Hz was applied to the LFP, particularly during two channel recording (for live comparison).

2.2. Surgery and imaging procedure

All surgical procedures were approved by the Animal Resources Center ethics committee of the University Health Network. An acute craniotomy was performed on a male Sprague Dawley (SD) rat and a flow chamber was mounted on the head, enabling introduction of K^+ channel blocker 4-AP and maintenance of the fluid level for a high magnification immersion objective lens. The details follow: The rat was anesthetized in an induction box using 5% isoflurane in a carrying gas of either 100% O_2 or 30% O_2 in N_2. The isoflurane concentration was reduced to 2.5% once the animal was secured within the ear bars. Bupivacaine (0.2 mL of 5 mg/mL) analgesic was injected into the scalp. The periosteum was removed. A ~4×6 mm oval bone chip was removed using a dental drill. The oval shape enabled more effective blood clearance. A continuous cold saline drip was used to mitigate the heat from drilling and was switched to a room temperature drip once the dura was exposed. The dura was carefully removed and the exposed brain was protected using absorbable gelatin sponge, enabling the mounting of a flow chamber to the skull using cyanoacylate. The chamber was built from rubber gaskets upon a stainless steel ring, and was oval shaped to facilitate blood removal. Isoflurane was always reduced to 1.5% prior to transferring the animal to the microscope stage. The exhaled CO_2, O_2 and isoflurane gases were measured using a capnograph (Capnomac II, Datex-Ohmeda GE Healthcare).

The calcium-sensitive fluorescent dye was injected via the glass electrodes using the picospritzer in 50 ms pulses with an internal pressure of 10 psi. Upon observation of sufficient dye uptake

Biomedical Optics EXPRESS

for visualization of individual cells at 4× magnification, the injection was stopped. The LPHR was aligned such that peak NIR illumination roughly overlapped with the region of maximum dye uptake. Once an ROI was selected, the objective lens was switched to a 20 – 40× water immersion objective for data collection. The FOV was adjusted such that both an arteriol and a venule were both visible. The saline in the chamber was exchanged with 5 mL of 1.5 mM of 4-AP over a 2 min period. Once one or more stable SLEs were observed in the LFP recording a 26 min imaging series was initiated. Following this imaging series, 2 mg/kg of LZP was administered via intraperitoneal (IP) injection. A second 26 min imaging series was then initiated. Following imaging, the animal was humanely euthanized using pentobarbital (100 mg/kg, IP injection). All drug administration time-points were noted in the electrical recording.

2.3. Analysis

The relative blood flow was calculated for LSCI using the speckle flow index (SFI) (as in ref. [16]). The Δ[HbR], $\Delta[HbO_2]$, and Δ[HbT] for IOSI where computed from the relative imaging intensities at R_{680}, R_{795}, and R_{850} (as in ref. [16]). During post-processing, ROIs were manually selected based on the perceived optimal signal-to-noise ratio (SNR). Due to the global nature of the seizure model and optical volume integration effects, changing the ROI did not produce qualitatively distinct results. The energy spectral density (ESD) of the LFP was calculated using a Hann window of length 1.5 s in steps of 0.2 s. The cardiac cycle phase and heart rate were calculated from the R-wave peaks in ECG recording. The R-wave centered profiles generated for each of the optical measures were set to zero mean per pulse (*i.e.,* $\sim$ 0.2 s) to limit the contribution from slower SLE associated changes. We calculated the SNR as $\sigma^2\{\langle x\rangle_{\in I}\}/\left\langle\sigma^2_{\in I}\{x\}\right\rangle$ where I is an interval rolling over all 1 s windows. A five frame rolling mean filter was applied to the LSCI and IOSI traces shown. For CSFDI, a three frame filter was used. The filters were not applied before SNR calculations or cardiac profile estimations. To correlate the electrographic SLEs with the optically measured parameters in an unbiased manner, we used the reduced noise generalized Teager energy operator (TEO) $\equiv x[n-1]\cdot x[n-2]-x[n]\cdot x[n-3]$ [19] applied to the LFP. This measure is equivalent to a point-wise approximation to the area under the frequency weighted ESD [20]. Consequently, both the frequency and amplitude of variation are proportionally weighted in this single value. We searched over different low-pass (LP) cut-off frequencies, f_c, applied to the TEO of the LFP to find the maximum Pearson's R^2. The time constant, $\tau_c = f_c^{-1}$, is the rate of signal response. We introduce the symbol, $\chi_c = \mathrm{LP}_c\{\mathrm{TEO}\{\mathrm{LFP}[t]\}\}$, for an optimally selected τ_c and, $\psi_\alpha = \mathrm{LP}_\alpha\{\mathrm{TEO}\{\mathrm{CSFDI}[t]\}\}$, for an *a priori* selected τ_α (α has no external definition). Piecewise linear interpolation was used to correct for differences in sampling rate.

3. Results

We continually measured blood flow, blood oxygenation, and $[Ca^{2+}]_i$ changes associated with *in vivo* SLEs, before and after intervention. The high sensitivity and dynamic range of the system allowed us to reliably track SLEs. We observed 142 SLEs in 13 different rodent imaging experiments. We observed an SLE median duration of 1.81 min [IQR = 0.45 min] prior to LZP and 0.98 min [IQR = 0.56 min] after LZP. The SNR associated with SLEs detection was approximately 15 for blood flow, 500 for blood volume and 30 for $[Ca^{2+}]_i$ oscillations. This imaging approach is suitable for a large FOV, but we typically focused on high-magnification imaging of smaller 200 μm or 400 μm FOV to investigate micro-vascular and cellular heterogeneity. We found that LZP perturbed SLE-dynamics in such a way as to suggest metabolic factors are the predominant moderator of this seizure model. The results demonstrate the usefulness of this multi-modality approach for investigating seizure dynamics and pharmacological intervention.

Biomedical Optics EXPRESS

3.1. Imaging recurrent seizures

Continual multi-modal imaging of recurrent SLEs over a 26 min period ($\approx 2^{14}$ repetitions of NIR six frame cycle) is shown in Fig. 2. After the topical application of 4-AP, we observed recurrent SLEs developing within ~ 10 min (see Fig. 2(a)–*i*). The onset of each SLE is marked by a negative shift in the LFP (*i.e.,* DC shift). After several seconds, the negative shift was arrested and high-amplitude oscillations began for 1-2 min. The termination of events were marked by a slower positive shift in the LFP. The high-amplitude oscillations decayed during the course of this positive shift. After the first SLE, events would typically re-occur with similar event-frequency and inter-event latency. However, in some instances, events would briefly stop and then re-initialize (see our prior conference proceeding [21]). No distinct frequency band, in the LFP-ESD, was associated with these SLEs (see Fig. 2(a)–*ii*).

Co-occurring within one second of the LFP-dip at SLE-onset, each optical imaging modality showed a change in the underlying measured parameter(s) (see Fig. 2(a)–*iii*-*v*). The LSCI based measurement of local cerebral blood flow began to rapidly increase (see Fig. 2(b)–*iii*). Furthermore, the diameter of arteries was observed to increase in the blood flow maps. For the example chosen here, the diameter of the artery increased by a factor of ~ 2× (see Fig. 2(a)–*vi* and Fig. 2(c)). This should correlate with an increase in blood volume and, as expected, the IOSI based measurement of local cerebral blood volume began to rapidly increase as well (see Fig. 2(b)–*iv*). The larger increase of HbO_2 relative to HbR was consistent with an influx of fresh blood due to vasodilation. However, the increase in blood volume was so dominant that the [HbR] versus [HbO_2] ratio was unchanged (*i.e.,* within 1.4 ± 0.2 %). The CSFDI based measure of $[Ca^{2+}]_i$ increased far more rapidly (% of max) at onset than blood flow and blood volume (see Fig. 2(b)–*v*). This rapid increase was also observed during LFP spikes. Consequently, as a measure of SLE-onset, $[Ca^{2+}]_i$ shows a higher sensitivity (*i.e.,* rapid increase at a true positive) but a dramatically reduced specificity (*i.e.,* many false positives). These changes in our optical parameters did not precede changes in the LFP.

Over the course of a SLE, blood flow and blood volume continually increased. Blood volume rose more rapidly than blood flow at SLE-onset (relative to the respective maximum values). However, the rate of blood volume rise leveled off more rapidly. The initial rapid rise in $[Ca^{2+}]_i$ after onset is followed by a gradual decline. During the event, the measured $[Ca^{2+}]_i$ began a series of high amplitude oscillations that are similar to the LFP oscillations with respect to temporal progression. The post-SLE decline of blood volume to pre-SLE values started approximately when both the DC and AC components of the LFP began to decline. However, blood flow started returning to baseline much closer to the end of all LFP related SLE-activity. Furthermore, during this post-SLE period, blood flow appears to correspond more strongly to LFP spikes. This is in contrast to the $[Ca^{2+}]_i$ signal which responded with greater duration to pre-SLE spikes than post-SLE spikes (see Fig. 2(b)–*v*).

3.2. Pharmacological intervention with an anti-convulsive agent

Upon LZP administration, we saw a change in the electrographic signature of the SLE, as shown in Figure 3. Firstly, the duration of SLEs decreased and the negative LFP-shift was reduced by approximately half. Additionally, the DC component began to decline sooner than high-amplitude oscillations, particularly for smaller DC shift SLEs. Moreover, the occurrence of SLEs increased in frequency by 77 ± 19% (> 0, $P = 0.005$, one sample t-test, $N_{rats} = 9$) with event magnitude and latency becoming less consistent. The example shown here (see Fig. 2(a) vs 3(a)) corresponds to an 82% increase in SLE recurrence rate (representative of average).

These changes in the LFP were associated with changes across optical modalities, which appear to mirror the new profile of SLEs (see Fig. 3(a)). However, there were notable differences in the way the profiles were changed. First, the increase in blood volume at SLE-onset became more distinct (see Fig. 3(a)–*iv*). Also, the maximum increase in blood volume shifted toward

Biomedical Optics EXPRESS

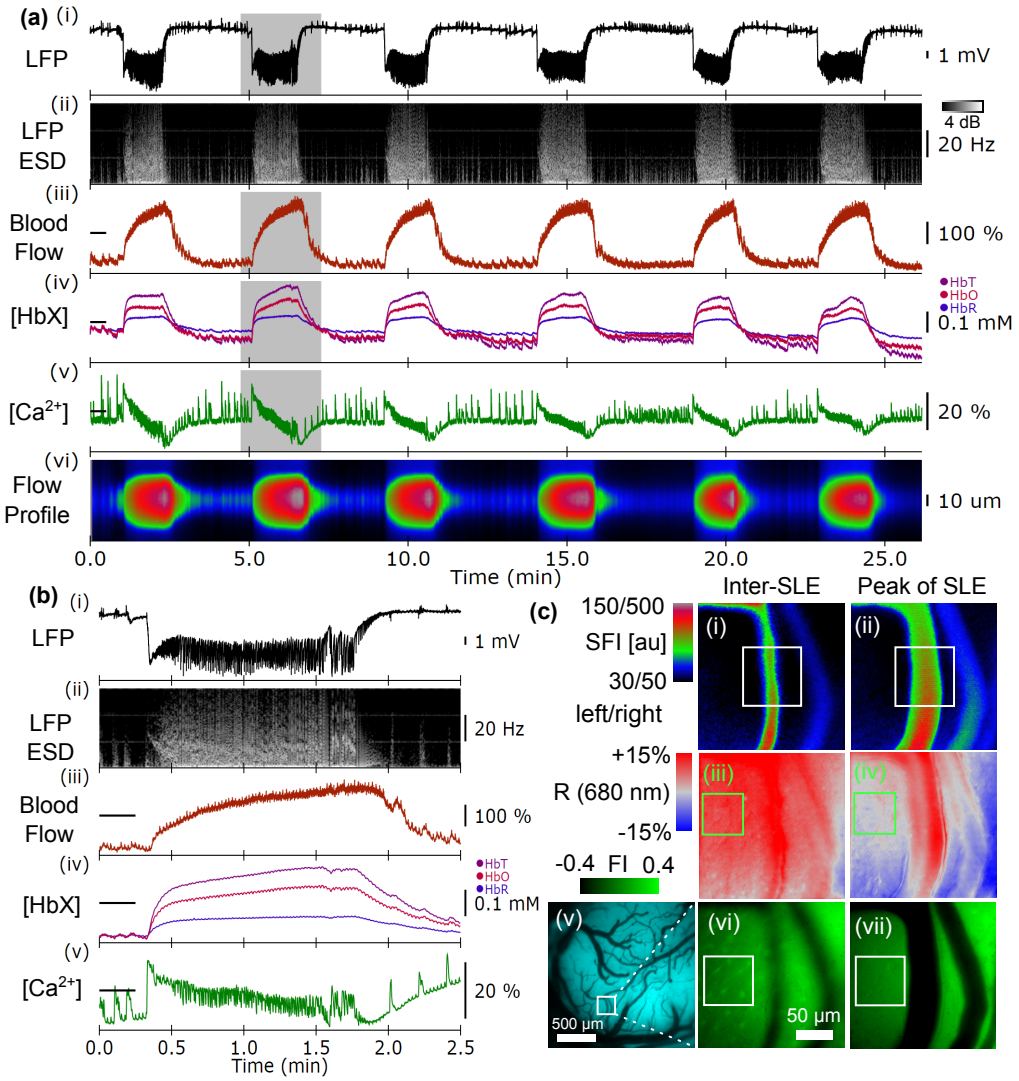

Fig. 2. High-speed multi-modal imaging of 4-AP induced SLEs. **(a)** 30 min after 4-AP application the measured (i) LFP, (ii) LFP-ESD, (iii) relative blood flow, (iv) $\Delta[HbO_2]$, $\Delta[HbR]$ and $\Delta[HbT]$ = blood volume, (v) relative $[Ca^{2+}]_i$, and (vi) blood flow cross section, across six SLEs. Horizontal black strip indicates baseline for plot. **(b)** Detailed view of the 2^{nd} SLE in grey window in (a). **(c)** Images of (i, ii) relative blood flow (in speckle flow index (SFI) units), (iii, iv) changes in 680 nm reflectance (~$\Delta[HbR]$), and (vi, vii) relative $[Ca^{2+}]_i$ from fluorescence intensity (FI) occurring between an SLE and at the peak of an SLE, respectively. (v) The larger FOV prior to dye injection. The ROIs used for (a & b)–*iii-v* are overlayed in (c)–*i,iii,vi* and also (c)–*ii,iv,vii*. The blood flow profile in (a)–*vi* was taken from the ROI in (c)–*i,ii*.

Biomedical Optics EXPRESS

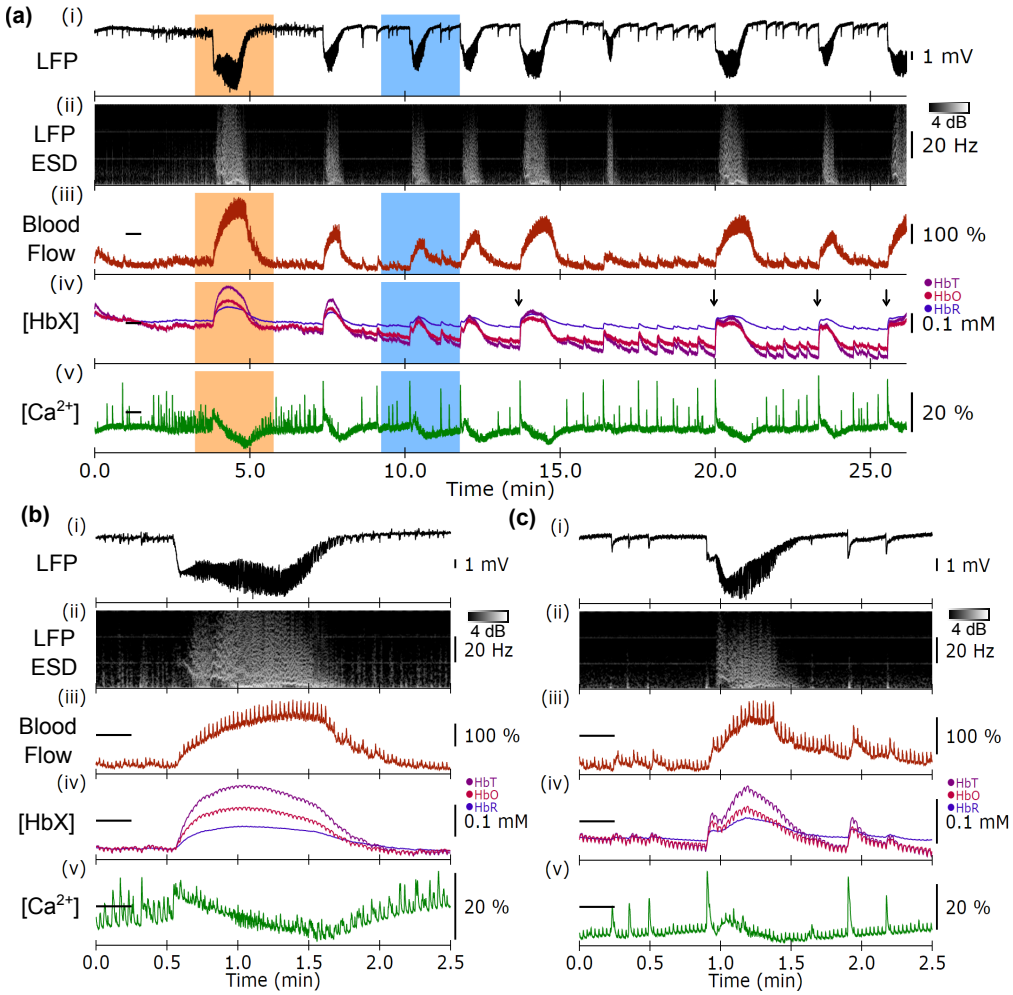

Fig. 3. Multi-modal imaging of SLEs after pharmacological intervention. **(a)** 5 min after LZP administration. (i-v) Use same correspondence as in Fig. 2, above. The four vertical arrows in (a)–*iv* mark higher distinction in the increase in blood volume at SLE-onset not matched by higher distinction in the increase in blood flow. **(b & c)** Detailed view of the 1st and 3rd SLEs from the orange and blue windows in (a), respectively. Multi-modal imaging of this rat prior to LZP administration is shown in Fig. 2. The ROIs shown in Fig. 2(c) were also used for all traces within this figure.

Biomedical Optics EXPRESS

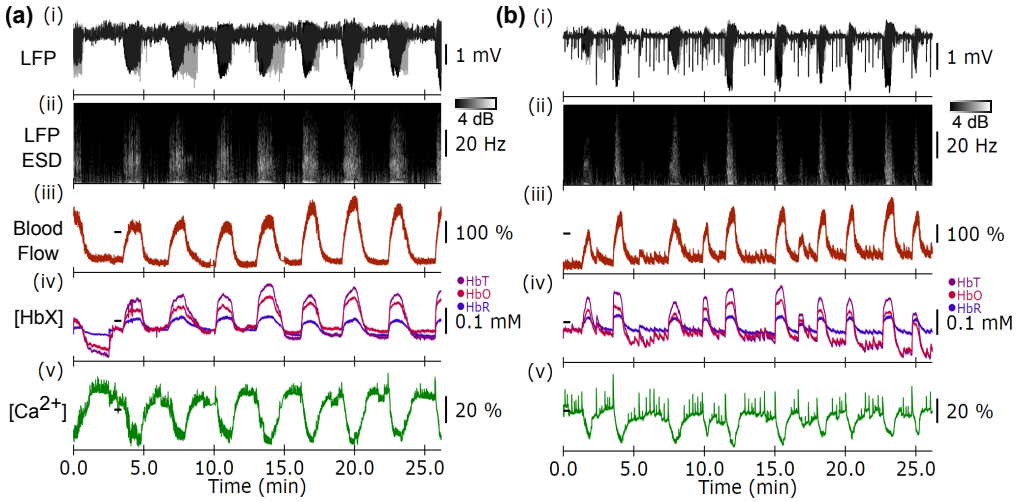

Fig. 4. Highest distinct SLE recurrence rate occurred under near-normoxic state. **(a)** Imaging series before and **(b)** after LZP administration. The (i-v) correspondence is the same as in Figs. 2 and 3. The second LFP in (a,b)–*i* is shown in grey.

the middle of each SLE (see Fig. 3(b-c)–*iv*). Conversely, the SLE associated blood flow profiles did not change noticeably with respect to the rate of increase at onset and the location of peak increase relative to the DC shift in the LFP (see Fig. 3(a-c)–*iii*). The blood flow profiles also appear to more closely mirror the more rounded SLE profile observed in the LFP. However, breathing-related artifacts in the blood flow, at approximately 1 Hz, became more predominant (see Fig. 3(b-c)–*iii*). The increase in magnitude of breathing artifacts is potentially indicative of metabolic stress. Relatedly, there was a gradual decrease in blood volume and [HbO_2] during the post-LZP time-period that was approximately 2× the rate before intervention (repeatedly observed). Again, this is suggestive of increased metabolic stress after intervention.

During post-LZP imaging, the CSFDI signal intensity had been significantly reduced due to photo-bleaching. However, IED and SLE-onset associated $[Ca^{2+}]_i$-spiking events were still clearly observable (indicating significant residual unbleached fluorescent dye) (see Fig. 3(a-c)–*v*). Interestingly, the high-amplitude $[Ca^{2+}]_i$ oscillations during SLEs were reduced in intensity and occurred only during the middle of SLEs (and sometimes in lower amplitude toward the end) (see Fig. 3(b-c)–*v*). In our large FOV implementation (see conference proceeding [22]) in which local photo-bleaching was less of a factor, the integrated-ESD of SLE associated $[Ca^{2+}]_i$-oscillations were also observed to be reduced.

Some of the smaller SLEs post-LZP involved a two-phase DC shift at SLE-onset (see Fig. 3(c)–*i,ii*). The SLE-onset $[Ca^{2+}]_i$ spike was associated with the first phase (see Fig. 3(c)–*v*). The blood flow and blood volume mirrored the two-phase DC shift (see Fig. 3(c)–*iii,iv*). Whether this is a result of inhibition or a consequence of exhaustion is beyond the scope of this work. However, these false starts indicate a potential investigative target for seizure perturbation.

3.3. *Reducing oxygen availability modified recurrence rate and calcium spiking*

Under a lower O_2 ventilation state (*i.e.,* 30% O_2 which is closer to ambient at 21%), we performed two repetitions of the imaging experiment, to assess the effect of O_2 availability on the observed dynamics. We refer to this ventilation state as the near-normoxic state since the O_2 level exceeds 21% (normoxia). The higher partial pressure offsets the reduced tidal volume associated with isoflurane anesthesia. The 100% O_2 ventilation state will be referred to as the high-hyperoxic

Biomedical Optics EXPRESS

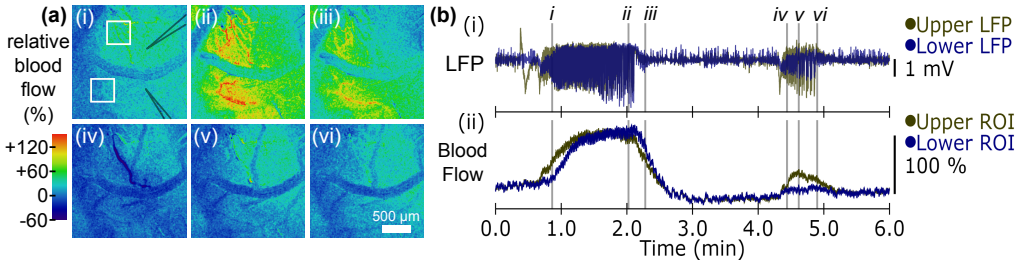

Fig. 5. Propagation of SLEs associated with high degree of correspondence in LFP. **(a)** Relative blood flow maps over a larger FOV showing (i-iii) propagation of a distinct SLE and (iv-vi) stagnation of a non-distinct SLE. **(b)** Comparison of (i) dual LFP recording and (ii) separate blood flow ROIs. Vertical grey bars indicate correspondence to (a)–*i-vi*.

state. The near-normoxic state did not noticeably change the HbR and HbO_2 ratio observed during SLEs relative to the high-hyperoxic state. However, in the near-normoxic example shown (see Fig. 4), we observed an increase in the recurrence rate of SLEs relative to the high-hyperoxic state. Specifically, before intervention, eight SLEs occurred within the acquisition sequence (see Fig. 4(a)), which is greater than the six SLEs seen in Fig. 2 (a). After intervention, eleven SLEs occurred within the same interval (see Fig. 4(b)) compared to the $7\frac{1}{2}$ SLEs seen in Fig. 3(a). Both the SLE duration and inter-SLE interval were reduced. In this instance, LZP administration increased the SLE recurrence rate by 79%, which is consistent with the experimental average of 77 ± 19%. Consequently, the near-normoxic state and LZP administration both increased the SLE recurrence rate with the combined effect appearing linear, and without producing qualitatively distinct behavior. We make no assertion as to the statistical significance of the increased SLE recurrence rate observed in the near-normoxic state compared to the high-hyperoxic state. We only assert that the high rate of distinct SLEs observed under near-normoxic state was not observed in the eleven comparable experiments under hyperoxia. The high-hyperoxic example presented (see Fig. 2 & 3) was close to the highest rate of distinct SLE recurrence observed within the hyperoxic experiments. The SLE recurrence rate of this near-normoxic example was 139% and 186% above the pre- and post LZP administration rates, respectively (including non-distinct SLEs which often have a short refractory period). These smaller SLEs were too rare and difficult to categorize for the estimation of population statistics.

In the other near-normoxic experiment (data not shown), the first SLE was 11.8 min in duration which was the longest observed, and started 6.8 min prior to imaging (observed in the LFP). Prior to SLE-termination, blood volume had returned to baseline levels, while blood flow persisted until the end of LFP-oscillations. After SLE-termination, blood volume increased in a manner similar to at SLE-onset with the exception that Δ[HbR] decreased just prior to SLE-termination. The refractory period of this SLE and its successor were longer than normal at 5min each. The two successive SLEs appeared similar to post-LZP administration SLEs but without a rapid onset. These two SLEs were also unique in that HbR declined more slowly than HbO_2 (by $\times 5.9$ for second SLE). In both near-normoxic state examples there was a large reduction in $[Ca^{2+}]_i$ spikes associated with the IEDs relative to SLE-oscillations. This relationship reversed after LZP administration with larger IED-spikes and reduced SLE-oscillations (see Fig. 4(a *vs.* b)–*iv*).

3.4. *Local variability in electrographic recording of seizure-like events*

In the near-normoxic example shown here (see Fig. 4), we see an activity difference between the two LFP recordings. This is particularly evident at the end of SLEs during the pre-LZP imaging sequence. Notably, the third and fifth SLEs continue to persist in one LFP recording for almost

Biomedical Optics EXPRESS

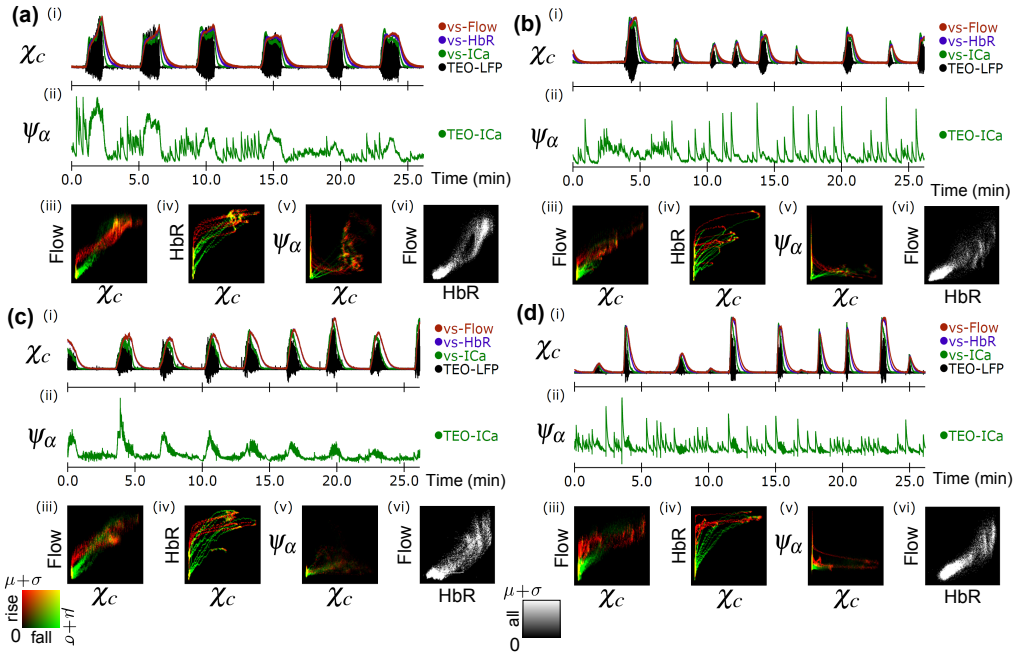

Fig. 6. Temporal correlation between optical parameters and χ_c during SLEs **(a)** prior to and **(b)** after LZP administration and **(c&d)** in the near-normoxic state. (i-vi) are the same for (a-d). (i) The χ_c maximally correlated with blood flow, HbR and CSFDI. (ii) The ψ_α parameter. Correlation plot between (iii) blood flow, (iv) HbR, and (v) ψ_α and their respective optimum χ_c. (iii-v) The red- and green-scales color scales indicate correspondence during increasing and decreasing χ_c, respectively. (vi) Correlation plot between blood flow and HbR.

1 min beyond the end of high-amplitude oscillation in the other LFP recording (see Fig. 4(a)–*i*). One LFP channel was more correlated with the optically-based measures, particularly at SLE termination. Consequently, it is possible to infer a different correspondence between the LFP and the optical signals for electrodes placed ≤ 500 μm apart. In the other near-normoxic state experiment, SLE associated high amplitude oscillations were consistent between LFP recording for large SLEs, but were inconsistent for shorter SLEs.

The dynamics of the LFP-dip at SLE-onset differed between the two LFP recordings, with the LFP-dip sometimes occurring in only one recording (observable in shorter time-scale view of data shown in Fig. 4(a,b)–*i*). This is in contradiction to the assertion that these are distinct seizure types (see reference [13]). It appears that the electrode closer to the SLE-onset zone undergoes a DC shift that is associated with onset. We recently found [22] that a discrepancy between LFP recordings was associated with the inability of seizures to propagate across a 2 mm FOV. A short time scale version of the result is shown in Fig. 5, highlighting the difference between two sequential SLEs. This pattern of a distinct and non-distinct SLE was repeated four times. The discrepancy was primarily in the lower frequency components of the signal at SLE-onset. Again, the amplitude of the LFP-oscillations only differ for the smaller SLEs. This experiment also exemplified the more rapidly decreasing blood volume observed after LZP administration.

Biomedical Optics EXPRESS

3.5. Correlation between imaging modalities and electrographic activity

We evaluated the correlation between the optical signals and electrographic activity using the χ_c parameter, which can approximate our blood flow and oxygenation measurements (see Fig. 6(a-d)–*i*). The ψ_α parameter provides a comparable measure for $[Ca^{2+}]_i$ (see Fig. 6(a-d)–*ii*). The standard error of the computed values of R^2 (Pearson's) are less then 0.45%, 0.78% or 0.56% when blood flow, HbR or ψ_α, respectively, are correlated with χ_c. The bound was computed from a transformation to a variable with a z-distribution. All pairwise comparisons in the data below are statistically distinct $P < 0.001$. The values of τ_c computed in the optimization procedure have no defined standard error. Arterial blood flow was the optically measured signal most highly correlated with χ_c (see Fig. 6(a)). The maximum R^2 were 93 % for blood flow, 82 % for HbR, and 31 % for ψ_α. However, the τ_c was larger for blood flow (at 22 s) than HbR (at 16 s) and ψ_α (at 6.4 s). This means that, despite blood flow having the strongest correlation with electrographic SLE-activity, its delay in response is also the longest. The recurrent SLEs trace a narrow figure-eight in the phase-space plots of blood flow versus χ_c (see Fig. 6(a)–*iii*). Conversely, the phase-space plot of HbR and χ_c show non-overlapping trajectories during the rising and falling phases (see Fig. 6(a)–*iv*). This indicated a mismatch in the SLE-onset coupling rate and SLE-termination decoupling rate of HbR relative to our measure of electrical activity χ_c. The low correlation of ψ_α and χ_c is largely due to differences in the duration of spiking events leading to no suitable low-pass filter pairings (see Fig. 6(a)–*v*). The large $[Ca^{2+}]_i$ spikes are apparent from the sharp vertical line in the phase-space plot. Also, the trajectories are far less discernible in this phase-space, particularly during SLE-onset. The strength of the correlation after intervention was reduced to 86 % for blood flow, 58 % for HbR, and > 1 % for ψ_α (see Fig. 6(b)). However, the optimum τ_c was reduced for both blood flow (to 16 s) and HbR (to 12 s). This indicates that the response was more rapid, although less consistent, after intervention. The optimum τ_c for $[Ca^{2+}]_i$ after intervention appeared to be an artifact of the IED-dominated $[Ca^{2+}]_i$ signal. Consequently, the τ_c of 6.4 s was used in Fig. 6(b)–*v*.

Optical parameter correlations under the near-normoxic state were slightly lower for blood flow (at 88 %) and HbR (at 65 %), and slightly higher for ψ_α (at 33%) (see Fig. 6(c)). After intervention, the correlations were reduced for blood flow (to 71%), HbR (to 57 %), and ψ_α (to < 1 %) (see Fig. 6(d)). Before intervention, the optimum τ_c was fairly similar for blood flow (at 18 s) and HbR (at 17 s) with ψ_α having a much shorter τ_c (at 4.9 s). Also, there was an absence of large $[Ca^{2+}]_i$ spikes associated with IED. This is most notable in the absence of the uncorrelated ψ_α verses χ_c spike (see Fig. 6(c)–*v*). After intervention, the τ_c were reduced for both blood flow (at 16 s) and HbR (at 12 s). Again, the τ_c for $[Ca^{2+}]_i$ was not measurable after intervention and the pre-LZP τ_c of 4.9 s was re-used in Fig. 6(d)–*v*.

The temporal relationship between blood flow and blood volume in the high-hyperoxic case is evident in the "loop" structure of the phase plot (see Fig. 6(a)–*vi*). The lower portion of the loop corresponds to SLE-onset and the upper portion to SLE-termination. The correlation remains high after intervention but the phase relationship is not as clear in the (see Fig. 6(b)–*vi*). The relationship is different in the near-normoxic state with a drifting "sickle" structure (see Fig. 6(c)–*vi*). This indicates that there is greater similarity between the SLE-onset and -termination trajectories but greater long term inconsistency (outside of constant drift which was removed). After intervention, the relationship appears much closer to the high-hyperoxic case (see Fig. 6(d)–*vi*).

3.6. Pulsation correction and vascular interaction dynamics

We were able to use the cardiac cycle phase information from the ECG signal to produce phase-synced optical signal profiles for improving the accuracy of blood flow and oxygenation measurements (see Fig. 7(a,b)). Cardiac pulsation correction for flow resulted in a 49 % and 94 % enhancement in SNR when applied to flow traces acquired before and after intervention, respectively. Before intervention, the flow pulsation profile distribution about a fixed-phase time

Biomedical Optics EXPRESS

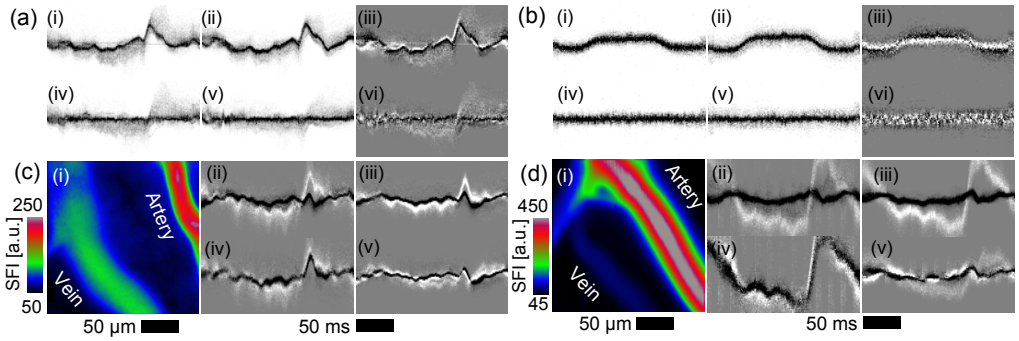

Fig. 7. Blood flow and HbR normalized value distributions along a cardiac cycle (profiles). **(a)** Blood flow profiles time centered on ECG R-wave (i) before intervention, (ii) after intervention, and (iii) before minus after intervention indicating profile change. In this grey-scale white is positive/before, black is negative/after and grey is no change. (iv-vi) The re-computed profiles from i-iii after subtraction of computed profile from signal. **(b)** Reflectance profile at 680 nm (~ Δ[HbR]). (i-vi) The same as in (a). **(c)** Comparison between small artery and large vein before and after intervention. (i) Blood flow map (temporally averaged). (ii) Artery minus vein before and (iii) after intervention. (iv) Artery and (v) vein before minus after intervention. **(d)** Comparison between large artery and small vein. (i-v) The same as in (c). For all plots the temporal window is 200 ms (*i.e.,* for 5 Hz heart rate) and vertical axis is 60 speckle flow index units (a, c, & d) or grey levels (b).

point changed from a downward to an upward skew (*i.e.,* the moment coefficient of skewness changed from −0.71 to +1.28) across the pulse maximum (see Fig. 7(a)–*i,iv*). The skew-effect size (not the skewness) was reduced after intervention. This reduction likely accounts for the larger SNR enhancement after intervention, as the profile distribution deviates less from the profile mode. As higher temporal resolution cannot change the distribution skew, improving upon the pulsation correction reported here will require a more sophisticated approach than profile estimation. The skew cannot be attributed to a mismatch in synchronization, since random effect would broaden the profile symmetrically. Also, this cannot be attributed to variability in heart rate as the skew is above the range of the distribution mode and heart rate was stable withing ±0.5 Hz. For reflectance at 680 nm (wavelength for which the pulsation dependence was largest) the pulsation correction improved the SNR by 17 % before and 19 % after intervention. The absence of skew in either estimated distribution (see Fig. 7(b)) explains the more consistent SNR improvement relative to blood flow. The larger SNR improvement for blood flow is a result of the more distinct profile which is expected given that blood flow is inherently pulsatile. The pulsation profile for CSFDI was almost random (data not shown), suggesting that the effect of pulsation is negligible with respect to our implementation of this modality. A slight phase delay in blood flow response after intervention can be seen in Fig. 7(a)–*iii*. We make no assertion to the statistical significance or neurological relevance of this delay. We only suggest that this system is capable of detecting these subtle effects through fast acquisition over tens-of-minutes.

In two different experiments the pulsation response of an artery and vein where contrasted. The first experiment had a large vein and a small artery in the left and right side of the FOV, respectively (see Fig. 7(c)–*i*). The discrepancy between the artery and vein flow profiles was larger before intervention than after, with a 64% larger difference between the artery and vein flow profile peaks before intervention than after (see Fig. 7(c)–*ii vs. iii*). After intervention, there was a decrease in arterial flow pulsation and an increase in venous flow pulsation (see Fig. 4(c)–*iv,v*) which indicates that the decrease in discrepancy is not attributed to one vessel type. The second experiment had a small vein and a large artery in the left and right side of the FOV,

Biomedical Optics EXPRESS

respectively (see Fig. 7(d)–*i*). The discrepancy between the artery and vein flow profiles was larger compared to the other experiment due to a greater arterial flow pulsation (see Fig. 7(d)–*ii & iii*). Strangely, the vein flow profile deceases during the arterial flow profile rise, suggesting that the large flow pulsation from the adjacent larger artery inhibits flow in the smaller vein. In this case, the difference between the artery and vein flow profile peaks was only 10% larger before intervention than after (see Fig. 7(d)–*ii vs. iii*). There was a slight phase delay in both the arterial and venous blood flow (see Fig. 7(d)–*iv & v*) similar to that observed in Fig. 7(a)–*iii*.

4. Discussion

Multimodal optical imaging is a promising approach for investigating SLEs. In this work, the physiological parameters measured by each of the three imaging modalities were highly correlated with the LFP associated SLE-activity. The observed changes in cerebral blood flow, blood volume and $[Ca^{2+}]_i$ during recurrent SLEs (*i.e.,* prior to intervention) were consistent with the qualitative observations from other systems and modalities [8–10, 13, 14]. Blood flow and blood volume were significantly enhanced during SLEs due to vasodilation (see Fig. 2). There were notable differences between the sensitivity and specificity of the different optically-measured parameters with respect to SLE identification, as shown in Figs. 2, 3, and 4. The change in blood volume showed the greatest specificity to SLEs, rapidly increasing at the onset of SLEs and decreasing immediately after SLE-termination (*i.e.,* with DC up-shift and AC-amplitude decay). Blood flow values had a lower specificity to SLEs and a longer latency at SLE-onset and -termination, with transient flow changes occurring during post-SLE small voltage spikes (*i.e.,* more sensitive to post-SLE spikes). The measured $[Ca^{2+}]_i$ rapidly increased to its maximum observed value at the onset of SLEs before proceeding into a series of high-amplitude oscillations. However, the high-sensitivity to voltage spikes between SLEs limited $[Ca^{2+}]_i$ values to serve as a robust measure of SLE-onset compared to blood volume and flow.

In this work, we also sought to demonstrate the benefits of multi-modal imaging in evaluating the effect of pharmacological intervention. The LZP model was chosen such that SLEs were not completely suppressed, enabling an investigation of SLE perturbation. After intervention, the duration and magnitude of SLEs were reduced, as shown in Fig. 3, with respect to all measured parameters. The consistency of SLEs (*i.e.,* similarity in magnitude and duration) was reduced, with a high correlation between the different modalities. Interestingly, the time interval between SLEs became significantly shorter and inconsistent in duration, yielding sporadic smaller SLEs. The reduced latency suggests that before intervention, larger SLEs exhaust the interconnected neurons sufficiently that another event is delayed while the metabolic availability returns to normal. As a consequence of reducing the size of SLEs, using LZP, we merely permit subsequent SLEs to re-occur sooner. Furthermore, we observed an increase in a breathing associated (~1 Hz) flow measurement after intervention and gradual decline in $[HbO_2]$. Combined, these results suggest that metabolic factors are a major contributor to the inability of LZP to rescue from seizure, if not administered early enough. The reduction in high-amplitude $[Ca^{2+}]_i$-oscillations associated with SLEs after intervention despite the continued presence of high-amplitude LFP-oscillations is suggestive that one component of the SLE was more effectively suppressed by LZP. This behavior is consistent with either synaptic fatigue through vesicle depletion or our assertion that metabolic factors are limiting recurrence.

The increased SLE recurrence rate observed (in Fig. 4) for the near-normoxic case consisted of both a shorter SLE duration and post-SLE recovery time. This suggests that SLEs are not able to sustain activity as long. However, as a consequence, tissue recovers quicker post-SLE. Conversely, in the event that a SLE does continue longer than expected, the post-SLE recovery interval is greatly expanded (data not shown). The greatly reduced $[Ca^{2+}]_i$-spiking associated with IEDs and their subsequent emergence during the suppression of high-amplitude $[Ca^{2+}]_i$-oscillations after intervention, suggests that with limited O_2 availability these two types of $[Ca^{2+}]_i$-activity

Biomedical Optics EXPRESS

are mutually exclusive. The persistence of SLEs in the absence of observable high-amplitude $[Ca^{2+}]_i$-oscillations suggests that these are correlated to SLE-activity but not a driving component in either the LFP-oscillations or NVC. This suggests that these oscillations are not caused by astrocytes or that the model of NVC involving astrocytic $[Ca^{2+}]_i$-waves contains an unknown redundancy. In the near-normoxic example (see Fig. 4), the observed discrepancy between LFP recordings during SLEs indicates that correlation with optical modalities must be done carefully. However, for our model, the LFP discrepancies appear to be localized to isolated SLEs or partially manifested SLEs (see Fig. 5 or ref. [22]). Moreover, the fact that one of two LFP recording was always a strong correlate to our optical measures indicates that within this 4-AP model there is a narrow range of LFP spatial variability.

The relationship between LFP associated SLE activity and NVC was assessed by introducing a new parameter χ_c (definition in Sec. 2.3). The optimized parameter χ_c (in Fig. 6) can well approximate either the blood flow and blood volume graphs (in Figs. 2, 3, 4). For CSFDI the ψ_α parameter was introduced, permitting a common temporal-scale for comparison. Treating the optically measured parameters as a delayed correlate to LFP associated SLE-activity allowed us to determine coupling response times, assess degree of correlation, and examine relative parameter dynamics (see Sec. 3.5). We found mismatch between coupled blood volume rising rate and the decay rate associated with the subsequent return to base-line, indicating that the blood volume relationship to SLE-activity is dictated by several factors operating on different time scales. This mismatch was most extreme in the post-LZP near-normoxic case (see Fig. 6(d)–*iv*). Conversely, blood flow showed greater similarity between the rates of SLE-onset and -termination, indicating that it is perhaps a more direct correlate to neural activity, despite a slower response time and increased post-SLE sensitivity. The correlative analysis also highlighted the effect of $[Ca^{2+}]_i$-spiking (see Fig. 6 (a,b,d)) and the absence of $[Ca^{2+}]_i$-spiking in the pre-LZP near-normoxic state (see Fig. 6(c)). The direct correlation between blood flow and Δ[HbR] revealed a strong cyclical relationship in the pre-LZP high-hyperoxic state. This represents a very predictable rhythm that may only be stable with excessive O_2 availability. Both the near-normoxic state and LZP typically reduced the strength of the correlation with optical parameters and the coupling response times. This is somewhat counter-intuitive, as one would expect an increase in correlation to be associated with a reduction in latency.

Cardiac pulsation is a source of noise for several imaging modalities, but is particularly problematic for LSCI, which directly measures blood flow. We tracked cardiac-cycle phase through the ECG measurement to enable high precision temporal registration of blood flow measurements (see Fig. 7(a)). This enabled both the estimation of cardiac-cycle blood flow profiles and the subtraction of such profiles to isolate the NVC related changes, yielding an SNR enhancement beyond what is reported in the literature [17]. However, we found that the blood flow profile had a distinct distribution asymmetry (skew) that was also asymmetric across the peak flow increase occurring during systole. This reveals a fundamental limit to pulsation correction for blood flow which cannot be surpassed with higher precision profile estimation. No profile skew was observed for IOSI but the impact of pulsation on SNR was far less (see Fig. 7(b)).

Despite pulsation resulting in a reduced SNR for LSCI in applications such as tracking NVC associated changes, we have demonstrated that it can measure subtle differences on a short time-scale (see Fig. 7). We found a difference, before and after LZP, in the artery versus vein peak flow pulsation ratio (see Fig. 7(c)). We see two potential explanations for this observation. One possible mechanism is that the vascular tone in other brain regions or cortical layers change after intervention. This could change the relative input and output resistance in each vessel to cardiac pulsation. Another possible mechanism is that the increased vessel strain during larger SLEs results in an increase in plasma (or simply water) crossing the vascular epithelium. This is similar to the mismatch in arterial versus venous flow which we previously demonstrated using LSCI in a model of blood-brain barrier (BBB) leakage [23]. The results from LSCI-ECG synchronization

Biomedical Optics EXPRESS

presented here suggest an opportunity to measure more subtle changes in BBB permeability. Moreover, there are a number of other correlates to neurovascular disease (such as endothelial inflammation or vessel stiffness) which could be investigated with this technique and simultaneous IOSI and CSFDI (or any number of fluorescence markers). Additionally, we observed a reduction in blood flow in a small vein during the pulsation associated increase in blood flow in a larger adjacent artery (see Fig. 7(d)). This suggests that the venule is partially restricted by pulsation which may affect its ability to adapt during NVC, or make it more vulnerable to occlusion. Consequently, this simple approach may be very promising for studying short time-scale vessel interaction dynamics. The temporal resolution of LSCI based pulsation profiles is fundamentally higher than those which can be generated using fast raster-scanning modalities such as TPLSM (or optical flow estimation with IOSI) as sequential scans (or frames) are required to estimate velocity, resulting in a temporal convolution of measurements.

There is significant room to expand upon the seizure perturbation approach investigated in this work. The impact of changing the timing, dosage or drug potency employed in the seizure model or pharmacological intervention have yet to be investigated. Particularly, the antiepileptic and GABAergic effects of isoflurane could influence our results. In addition, modifying other factors such as blood glucose levels could provide further insight into the main factors that contribute to the apparent exhaustion observed (see Fig. 3). Lastly, since the action spectrum of most available optogenetic (and opto-chemical) probes are in the visible spectral region, NIR imaging can continuously monitor NVC associated with visible wavelength activation of optogenetic probes without unintentional stimulation. Consequently, together with selective optical stimulation of specific neurons, it should be possible to use this multi-modal imaging approach to correlate the effects of drugs on specific cellular pathways.

5. Conclusion

We demonstrated continuous full-field multi-modal imaging over tens-of-minutes, and the first application of multi-modal imaging for seizure evaluation that included fast high-resolution blood flow imaging. This is the first study, to the best of our knowledge, that evaluated the effect of pharmacological intervention on SLEs using multi-modal imaging. The results of this study suggest that metabolic factors may be major contributors to the limited ability of some drugs to effectively rescue from seizure. Furthermore, in conditions where a full rescue from a seizure is not possible, drug administration may be detrimental to recovery. We provide an initial approach to assessing the relationship between optical correlates of seizure and electrical activity, revealing blood flow as a stronger correlate to neural activity and blood volume as a higher precision measure for SLE-onset detection. Synchronization with cardiac pulsation allowed us to observe interaction effects between vessel types that were previously uncharacterized.

Funding

National Sciences and Engineering Research Council (NSERC) (RGPIN-355623-08); Canadian Institutes of Health Research (CIHR) (CPG-121050 and MOP-119603); Connaught Fund (498042); MITACS (IT02018).

Acknowledgment

The authors would like to thank Iliya Sigal, Vanessa Breton and Dr. Liang Zhang for useful discussions, and Dr. Mary Hibbs-Brenner from Vixar Inc. for assistance in VCSEL packaging.